ACS APPLIED ENERGY MATERIALS

www.acsaem.org Article

Improved Photoelectrochemical Hydrogen Gas Generation on Sb_2S_3 Films Modified with an Earth-Abundant MoS_x Co-Catalyst

Moisés A. de Araújo, Magno B. Costa, and Lucia H. Mascaro*

Cite This: ACS Appl. Energy Mater. 2022, 5, 1010−1022 Read Online

ACCESS | Metrics & More | Article Recommendations | Supporting Information

ABSTRACT: Antimony(III) sulfide (Sb_2S_3) has recently emerged as an outstanding potential photoelectrode due to its superlative optoelectronic properties for light-driven water splitting application. However, the occurrence of the recombination process in this material is regarded as one of the main limiting factors to date. Herein, we greatly suppressed the occurrence of recombination and improved carrier transfer via photoelectrodepositing an earth-abundant MoS_x co-catalyst over Sb_2S_3 films. The Sb_2S_3/MoS_x films displayed a remarkable 2-fold increase of their photoresponse for H_2 generation and also resulted in shifting the onset potential approximately 100 mV to less negative values. Based on an in-depth analysis of the transients' photocurrent density, the enhanced photoresponse was assigned to a smaller probability of the electron−hole recombination process, as noted from the substantial reduction of the accumulated negative charge density values at the surface of the Sb_2S_3 films. The minimization of carriers recombination was also verified from the decrease of the charge transfer resistance values by approximately 2-fold for the Sb_2S_3/MoS_x films. Additionally, Sb_2S_3/MoS_x featured an increase of the space charge thickness, which suggests an improvement of carrier separation or a minimized recombination process due to the enlarged gradient of the (quasi-)Fermi level in the space charge region of the Sb_2S_3 films.

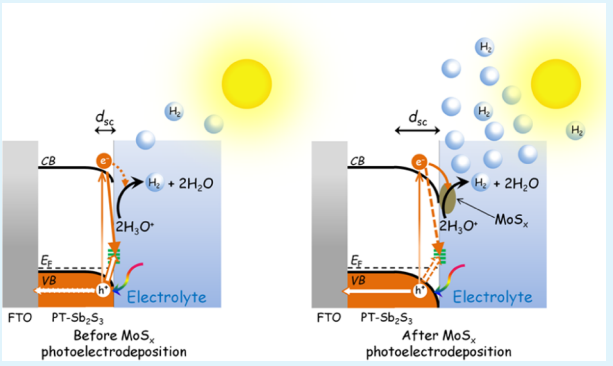

KEYWORDS: *antimony sulfide, molybdenum sulfide, water splitting, photoelectrochemical cells, solar energy*

INTRODUCTION

The chemist Antoine-Laurent de Lavoisier is probably one of the pioneers in studying the decomposition of water into dihydrogen (H_2) and dioxygen (O_2).[1] This initial study was particularly important at that time, as it had provided compelling evidence to rule out the phlogiston theory.[2] Today, the study of water splitting is highly regarded as it is considered a sustainable approach to obtain H_2, which is a clean energy carrier with great potential to be one of the main sources of energy in the future. Particularly, light-driven water splitting in photoelectrochemical (PEC) cells is considered a promising approach to convert solar energy into hydrogen fuels.[3] In this way, a variety of semiconductor films have been assessed as photocathodes to solar-driven water splitting in an efficient and stable manner. Recently, earth-abundant and nontoxic antimony(III) sulfide (Sb_2S_3) film has increasingly gained considerable attention as a new alternative photocathode for H_2 generation in PEC cells. Such attention is due to its unique optoelectronic properties, such as its narrow indirect optical bandgap (E_g) of 1.6 eV and high absorption coefficient (α) of 10^4−10^5 cm^{-1} (for photons with energy greater than its E_g).[4] Additionally, Sb_2S_3 has a considerable theoretical maximum photocurrent density ($\Delta j_{ph,max}$) of ca. 24.5 mA cm^{-2} and a substantial theoretical solar-to-hydrogen efficiency of 28%,[5] which are desirable for practical application. It is also worth mentioning that Sb_2S_3 is a semiconductor material having intrinsic n- or p-type conductivity, suggesting a versatile material that can be employed as a photoanode or photocathode in PEC cells, respectively.[6] Alongside the dual conductivity, Sb_2S_3 features suitable band edge positions that straddle both water reduction and oxidation potentials for PEC H_2 and O_2 generation, respectively.[5]

It is fair to mention that albeit Sb_2S_3 has all of these suitable properties for the light-driven hydrogen evolution reaction (HER), this material can feature a superhydrophobic surface, which is problematic to generate H_2 in aqueous media.[7] To tackle the hydrophobicity issue, recently, we have reported a novel approach based on fast dinitrogen (N_2) plasma treatment that enabled a change in the surface of the Sb_2S_3 films from superhydrophobic to hydrophilic. Besides the hydrophobic issue, the occurrence of the recombination

Received: October 27, 2021
Accepted: January 5, 2022
Published: January 13, 2022

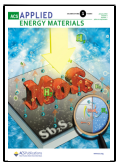

https://doi.org/10.1021/acsaem.1c03374
ACS Appl. Energy Mater. 2022, 5, 1010−1022

Scheme 1. Schematic Representation for the Preparation of Sb_2S_3 Films and Their Superficial Modification

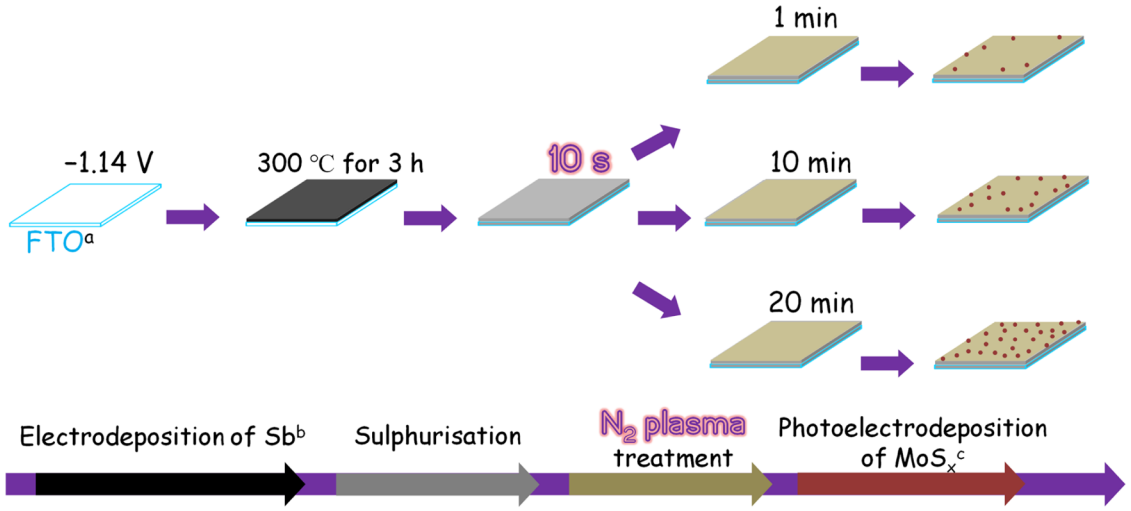

[a] Cleaned and hydrophilised glass-coated FTO.
[b] Bath: 6.0 mmol L^{-1} $K_2Sb_2(C_4H_2O_6)_2$ dissolved in 0.1 mol L^{-1} $KNa(C_4H_4O_6)$ pH 6. Deposition charge density: −500 mC cm^{-2}.
[c] Bath: 2.0 mmol L^{-1} $(NH_4)_2MoS_4$ dissolved in 0.5 mol L^{-1} Na_2SO_4 pH 5. Deposition potential: −0.35 V.

process[8] and the possibility of Sb_2S_3 films undergoing photocorrosion[9] in aqueous media are still recurring problems that need to be dealt with. In an attempt to overcome these deleterious factors, it has been demonstrated that employing a heterostructure approach, such as SnS/Sb_2S_3 and Co_3O_4/Sb_2S_3, can potentially improve the photoelectroactivity of Sb_2S_3 films.[10,11] Another promising strategy to circumvent the aforementioned problems is to deposit HER co-catalyst nanoparticles on the surface of Sb_2S_3 films, as it can effectively minimize carrier losses by recombination that occurs under operating conditions. Employing a HER co-catalyst over a semiconductor film also allows improvement to the interfacial kinetics of carrier transfer and decrement in the overpotential of the system for the occurrence of the HER.[3]

Compared to the costly, and scarce, platinum (Pt), co-catalysts based on molybdenum disulfide (MoS_2) and amorphous molybdenum sulfide (MoS_x, x = 2 or 3) have gained considerable attention in the last decades for being less costly, earth-abundant, and having an outstanding catalytic activity to drive the HER.[12,13] Additionally, MoS_x particularly also proves to be advantageous in terms of economical synthesis as it does not require annealing, which is usually necessary to obtain crystalline MoS_2.[14] MoS_x can be prepared over a semiconductor material by photoelectrodeposition, and that can be carried out potentiostatically[15] or galvanostatically.[16] The photoelectrodeposition stands advantageously as it allows selectively depositing the co-catalyst at locations where photogenerated electrons are readily available on the semiconductor surface. This ensures greater efficiency in the use of the co-catalyst since it will be placed at locations where the PEC HER most likely takes place.[17] The MoS_x photoelectrodeposition procedure on a p-type semiconductor film (photocathode) consists of initially placing the film in a solution containing the tetrathiomolybdate ion ($[MoS_4]^{2-}$) precursor. Once this system is under illumination and polarization, the following events occur: (i) absorption of light by the photocathode followed by the generation of an electron in the conduction band (e^-_{CB}) and holes in the valence band (h^+_{VB}); (ii) migration of the e^-_{CB} to the photocathodel electrolyte interface; and (iii) transfer of the e^-_{CB} to reduce $[MoS_4]^{2-}$ ions to MoS_2 (cf. eq 1), which is subsequently assembled, preferably, at the active sites of the photocathode surface.[3,15]

$$[MoS_4]^{2-}_{(aq)} + 2H_2O_{(l)} + 2e^-_{CB} \rightarrow MoS_{2(s)} + 2HS^-_{(aq)} + 2OH^-_{(aq)} \quad (1)$$

Regarding the photoelectrodeposition of MoS_x nanoparticles over Sb_2S_3 films for PEC H_2 generation, to the best of our knowledge, no such study has been reported yet. The studies in the literature about the Sb_2S_3/MoS_x films assess this system as an anode for the application of sodium-ion batteries.[18,19] Only recently, efforts have been made on improving the photocurrent density (Δj_{ph}) response for the HER on Sb_2S_3 film via deposition of Pt nanoparticles over Sb_2S_3-based heterostructures, namely, $CuInS_2$/Sb_2S_3/Pt[20] and Sb_2S_3/CdS/TiO_2/Pt.[5]

On the strength of what has been said and aiming to improve the photoelectroactivity of Sb_2S_3 films for H_2 generation, we herein propose the novel system based on plasma-treated Sb_2S_3 (PT-Sb_2S_3) films superficially modified with nanoparticles of MoS_x. Both Sb_2S_3 and MoS_x were obtained by electrodeposition, which is well known for being economical, simple (not requiring sophisticated systems/equipment), and easily scalable. Particularly, we investigated in this work the effect of MoS_x photoelectrodeposition time on the photoelectroresponse of the PT-Sb_2S_3/MoS_x system for the HER. We demonstrated that the MoS_x photoelectrodeposition time did not significantly influence the photoelectroresponse of PT-Sb_2S_3/MoS_x. Nevertheless, the presence of MoS_x revealed substantial improvement of the photoelectrocatalytic properties of PT-Sb_2S_3 films for the HER, as observed by the improvement of Δj_{ph} response and shifting of the onset potential (E_{on}) toward less negative values. Furthermore, we demonstrated that the presence of MoS_x nanoparticles enabled a decrease of carrier recombination on the surface of PT-Sb_2S_3

https://doi.org/10.1021/acsaem.1c03374
ACS Appl. Energy Mater. 2022, 5, 1010−1022

films as well as a noticeable reduction in charge transfer resistance (R_{ct}) at the semiconductor|electrolyte interface.

EXPERIMENTAL SECTION

Synthesis and Surface Modifications of the Sb_2S_3 Films. The synthesis of the Sb_2S_3 films over glass-coated fluorine-doped tin oxide (FTO) substrate can be found in our previous work.[7] Briefly, the synthesis of the Sb_2S_3 films consisted of initially electrodepositing Sb films potentiostatically at −1.14 V vs $Ag/AgCl/Cl_{(sat.\ KCl)}^-$ with a deposition charge density of −500 mC cm^{-2}. The electrodeposition bath was a freshly made solution of 6 mmol L^{-1} $K_2Sb_2(C_4H_2O_6)_2$ dissolved in 0.1 mol L^{-1} $KNa(C_4H_4O_6)$ at pH 6 (pH adjusted with diluted H_2SO_4), which was the supporting electrolyte and complexing agent. The as-electrodeposited Sb films were subjected to a sulfurization treatment at 300 °C for 3 h under a sublimated S atmosphere to obtain the Sb_2S_3 phase. As depicted in our latest work,[10] the employed sulfurization system consisted of a partially closed cylindrical glass, which contained the samples and 0.1 g of elemental S powder as the sulfide source. This closed cylindrical glass was placed in a tubular furnace (EDGCON 5P) with a flux of Ar gas.

Then, the Sb_2S_3 films were treated under N_2 plasma for 10 s in a plasma cleaner equipment (Zhengzhou CY-P2L-B). As reported in our latest work, the purpose of the plasma treatment was to turn the superhydrophobic surface of the Sb_2S_3 films into hydrophilic, which is an essential condition for efficient H_2 production via water splitting.[7]

Sequentially, the surface of the PT-Sb_2S_3 films was modified with nanoparticles of MoS_x co-catalyst via the photoelectrodeposition method. This experiment consisted of front-illuminating the PT-Sb_2S_3 films and concomitantly applying −0.35 V vs $Ag/AgCl/Cl_{(sat.\ KCl)}^-$ (the deposition potential was determined from cyclic voltammetry analyses as shown in Figure S1) during different deposition times, i.e., 1, 10, and 20 min, and the samples were labeled as PT-Sb_2S_3/(1, 10, or 20 min)-MoS_x.

The PEC system setup was composed of a solar simulator (Oriel LCS-100 with a 100 W Xe lamp coupled to an AM1.5G filter) with an irradiance of 100 mW cm^{-2}, and a three-electrode cell having a quartz window. The working electrode (WE) was the PT-Sb_2S_3 films, while the reference (RE) and counter electrodes were an $Ag/AgCl/Cl_{(sat.\ KCl)}^-$ and Pt plate, respectively. All potential values are quoted with respect to this RE (197 mV vs reversible hydrogen electrode (RHE) at 25 °C) whose potential was constantly checked before and after each measurement, and its value did not show any significant variation. The employed deposition bath was a freshly prepared solution of 2.0 mmol L^{-1} $(NH_4)_2MoS_4$, as Mo and S precursors, dissolved in 0.5 mol L^{-1} Na_2SO_4 at pH 5 (pH adjusted with diluted H_2SO_4), which was the supporting electrolyte. Prior to every experiment, this solution was saturated with N_2. The MoS_x deposition bath was adapted from the methodology reported by Tran et al.[15] A summary of all of the steps involved in the preparation of the films is depicted in Scheme 1.

Physical and Chemical Characterization of the Films. The crystalline structure of the films was analyzed using an X-ray diffractometer (Shimadzu XRD-6000) with Cu K-L_3 ($K\alpha_1$) radiation (1.54 Å). The diffractograms were recorded at a scan speed of 0.20° min^{-1} and a sampling pitch of 0.02°. The diffraction peaks indexations were handled with the Crystallographica Search-Match (version 2, 1, 1) software.[21] The films' morphological investigation was carried out on a high-resolution field emission scanning electron microscope (FE-SEM, ZeissSupra 35). The chemical analysis of the films was performed employing an energy-dispersive X-ray spectrometer (Bruker XFlash 6|60 detector) coupled with the FE-SEM (Philips XL-30). For a further chemical understanding of the films, an X-ray photoelectron spectrophotometer (Scienta Omicron) with a monochromatic Al K-L_3 ($K\alpha_1$) radiation (1486.7 eV) was employed. The high-resolution spectra of the C 1s, N 1s, S 2p, Mo 3d, and Sb 3d core levels were recorded with an energy step of 0.05 eV at a pass energy of 50 eV. For the data processing, all of the spectra were calibrated with the C 1s peak at 284.8 eV. The spectra background was fitted using a U3 Tougaard function, and the peaks were fitted with a Gaussian−Lorentzian lineshape, namely, LA ($1 \le a \le 10$, $0 \le b \le 15$, $80 \le m \le 500$), where a and b are the Lorentzian contribution terms and m is the width of the Gaussian. All of the spectra analyses were handled with the CasaXPS (version 2.3.19PR1.0) software.[22] The estimation of the optical E_g was achieved utilizing an ultraviolet−visible−near-infrared (UV−vis−NIR) spectrophotometer (Varian Cary 5) at diffuse reflectance mode.

Photoelectrochemical Assessment of the Films. The PEC assessment study aimed to evaluate the photoelectroactivity of the synthesized films for H_2 generation via light-driven water splitting. For this study, the main parameter used to assess the films' photoelectroactivity for the HER was the generated cathodic Δj_{ph} signal, which is directly proportional to the amount of H_2 generated. This parameter was obtained from the linear sweep voltammetry curves both in the dark and under illumination, which was scanned from the open-circuit potential (E_{oc}) to −0.40 V at a scan rate of 50 mV s^{-1}. Additional experiments based on chronoamperometry measurements at −0.2 V (potential for the HER at pH 0.6) and under chopped light were carried out to analyze the dynamics of the photogenerated carriers.

For a further understanding of the films' photoelectroactivity, electrochemical impedance spectroscopy (EIS) experiments were conducted. These experiments were performed under constant illumination, and the films were polarized at −0.2 V, which is the potential for the HER at pH 0.6. The impedance spectra were obtained in a frequency range of 100 kHz to 0.1 Hz and a root mean square (rms) amplitude of 10 mV. The spectra were modeled to an equivalent electric circuit using the ZView (version 3.1c) software. As an additional characterization of the films, the Mott−Schottky plots were obtained to determine the flatband potential (E_{fb}) and semiconductor conductivity type (n- or p-type). The experiments were conducted applying a sinusoidal excitation signal of 10 mV_{rms} and a frequency of 1.0 kHz, which is the most used in the literature for the Sb_2S_3.[5,23] The applied potential range was from the E_{oc} to −0.20 V (divided into 15 points) with an equilibrium time of 1 min prior to every applied potential.

All of these experiments were performed employing the PEC system setup described at the beginning of this experimental section and using a N_2-saturated solution of 1.0 mol L^{-1} H_2SO_4 at its natural pH of 0.6. We have chosen this electrolyte because MoS_x is more effective to electrocatalyze the HER in strong acid media (pH 0 or 1).[16] The WE, namely, the Sb_2S_3/(1, 10, or 20 min)-MoS_x films, was front-illuminated.

RESULTS AND DISCUSSION

Prior to the investigation of the Sb_2S_3/MoS_x films for PEC H_2 generation, initially, we assessed whether to photoelectrodeposit MoS_x over the untreated or plasma-treated Sb_2S_3 film. In this way, MoS_x was then deposited onto untreated Sb_2S_3 (labeled as UT-Sb_2S_3) and PT-Sb_2S_3 films polarized at −0.35 V and under illumination for 10 min. The photoelectroactivity of UT-Sb_2S_3/MoS_x and PT-Sb_2S_3/MoS_x films for H_2 generation was assessed by linear sweep voltammetry both in the dark and under illumination (see Figure S2). Compared with the UT-Sb_2S_3/MoS_x film, the PT-Sb_2S_3/MoS_x film displayed an overwhelmingly higher cathodic Δj_{ph} response over the entire range of potential values. Taking the cathodic Δj_{ph} value at −0.2 V, which is the potential for the HER at pH 0.6, the UT-Sb_2S_3/MoS_x and PT-Sb_2S_3/MoS_x films presented values of −0.02 and −1.00 mA cm^{-2}, respectively. The diminished photoresponse for UT-Sb_2S_3/MoS_x film is due to the superhydrophobic nature of the UT-Sb_2S_3 film, as previously reported in our latest work.[7] This superhydrophobic behavior for UT-Sb_2S_3 film also resulted in impeding the deposition of MoS_x. This was verified by the absence of the characteristic peaks of MoS_2 in the Mo 3d spectrum (see Figure S3), which only displayed peaks corresponding to S 2s[24]

https://doi.org/10.1021/acsaem.1c03374
ACS Appl. Energy Mater. 2022, 5, 1010−1022

assigned to probably Sb_2S_3. The superhydrophobicity of the UT-Sb_2S_3 film compromised the deposition of MoS_x as it prevented $[MoS_4]^{2-}$ species from reaching the UT-Sb_2S_3 surface. Based on the general electrodeposition steps,[25] the attraction of $[MoS_4]^{2-}$ ions onto the film's surface is critically important for the subsequent deposition steps, namely, adsorption of $[MoS_4]^{2-}$ species followed by their discharge. Since the surface of the UT-Sb_2S_3 film is highly hydrophobic, none of these aforementioned deposition steps took place due to the poor affinity of $[MoS_4]^{2-}$ ions to be drawn to the surface of the UT-Sb_2S_3 film.

In light of the impossibility to deposit MoS_x on UT-Sb_2S_3 films, we decided to perform the deposition of this compound over the PT-Sb_2S_3 films, and for this study, the deposition time was systematically investigated. The PT-Sb_3S_3 and PT-Sb_3S_3/(1, 10, or 20 min)-MoS_x films initially were characterized in terms of their physical, chemical, and optical properties, as presented hereinafter.

Physical, Chemical, and Optical Characterization of the Films. The microstructural nature for bare PT-Sb_2S_3 and PT-Sb_2S_3/(20 min)-MoS_x films were assessed employing X-ray diffraction (XRD) patterns, and the results are displayed in Figure 1. For this analysis, we only employed the longest MoS_x

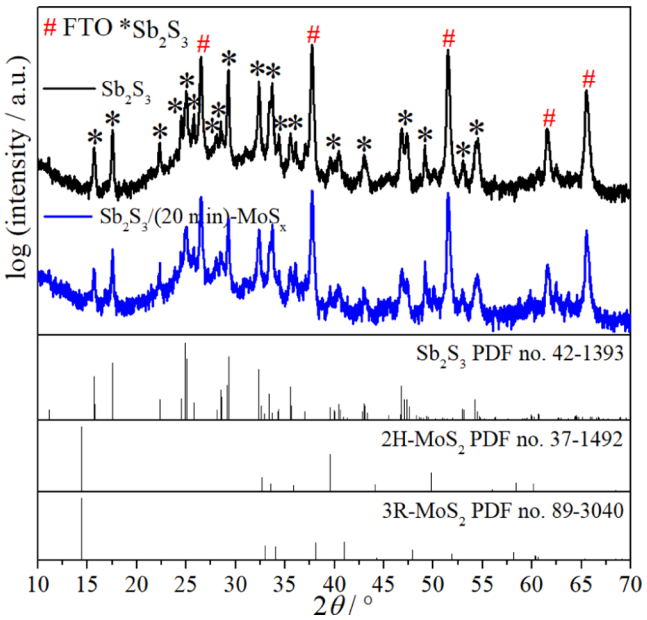

Figure 1. XRD patterns for PT-Sb_2S_3 and PT-Sb_2S_3/(20 min)-MoS_x films. Reference patterns for Sb_2S_3 (Powder Diffraction File (PDF) no. 42-1393),[26] 2H-MoS_2 (PDF no. 37-1492),[27] and 3R-MoS_2 (PDF no. 89-3040)[28] are also shown. The diffraction peaks labeled with hashes (#) are assigned to the SnO_2 (PDF no. 41-1445)[29] from the FTO coating on a glass substrate.

photoelectrodeposition time (20 min) as it could provide facilitation in the detection of the MoS_x due to the greater amount of the deposited MoS_x.

According to Figure 1, all of the diffraction peaks labeled with asterisks (*) were indexed to crystalline orthorhombic Sb_2S_3 phase with a *Pbnm* space group for both samples. For the superficially modified film, we expected to photoelectrodeposit the MoS_2 compound; however, we have not observed any additional diffraction peaks referring to any of the main MoS_2 phases, namely, 2H and 3R phases.[30] This result means that the photoelectrodeposition of MoS_2 under these conditions may have led to an amorphous or nanocrystalline material formation (referred to as MoS_x), which is consistent with studies in the literature that (photo)electrodeposited MoS_x is usually amorphous.[31,32]

The PT-Sb_2S_3 and PT-Sb_2S_3/(1, 10, or 20 min)-MoS_x films were also characterized in terms of their morphology by scanning electrons microscopy (SEM) micrographs as shown in Figure 2. The morphology of the PT-Sb_2S_3 film seems to feature round-shaped agglomerations having particle lengths of approximately 325 nm, as shown in the particle size distribution histograms of Figure S4. For the Sb_2S_3/(1 min)-MoS_x film, despite not observing any obvious modifications, we believe that very small clusters/particles of MoS_x were deposited all over the film as there was a significant improvement of the film's photoelectrocatalytic properties (further presented below). Increasing the MoS_x photoelectrodeposition time for 10 and 20 min resulted in substantial superficial modification of the films compared to the bare one, which suggests that the MoS_x may have been deposited in a greater amount on the PT-Sb_2S_3 films. As also indicated in the inset of Figure 2, it is noted that the round-shaped agglomerations of the PT-Sb_2S_3 films seem to have a rougher surface once modified with the MoS_x photoelectrodeposited for 10 and 20 min. Based on these results, it is evident that increasing the MoS_x photoelectrodeposition time significantly changes the films' surface, as well as leading to thorough coverage of the PT-Sb_2S_3 films.

Aiming to chemically characterize the PT-Sb_2S_3 and PT-Sb_2S_3/(1, 10, or 20 min)-MoS_x films, energy-dispersive X-ray spectra (EDS) were recorded for those films and are depicted in Figure S5. As noted, the EDS spectrum for the PT-Sb_2S_3 film displayed the Sb and S characteristic peaks, which provided an S/Sb atomic ratio of 1.6, as listed in Table S1 and Figure S6. Albeit EDS is a semiquantitative technique, the obtained S/Sb atomic ratio is very close to the expected stoichiometric composition, i.e., S/Sb = 1.5. Regarding the PT-Sb_2S_3/MoS_x films, the Mo K-L_3 ($K\alpha_1$) peak at 17.5 keV[33] (signaled by a red vertical line in the inset of Figure S5) was not observed. Such a result suggests that even though the films were superficially modified, as seen from SEM images in Figure 2, the deposited amount of MoS_x is very low. Moreover, as shown in Table S1 and Figure S6, the atomic percentage of Sb and S continuously decreases over the MoS_x photoelectrodeposition time, implying that the detection of such elements is hindered due to the deposited overlayer. To verify the presence and homogeneity distribution of the photoelectrodeposited MoS_x over the film's surface, EDS elemental mapping images were obtained and are shown in Figure 3. For the superficially modified films, we were able to confirm the presence of the MoS_x for all of the photoelectrodeposition times and that this compound was evenly distributed over the PT-Sb_2S_3 films. Additionally, for the bare PT-Sb_2S_3 film, the Sb and S elements are homogeneously distributed throughout the film.

Further chemical analyses of the films were performed by X-ray photoelectron spectroscopy (XPS) to confirm the presence of Sb, Mo, and S elements as well as their oxidation states and chemical bonding. For this study, the XPS spectra (see Figure 4) of the bare PT-Sb_2S_3 film was obtained including the ones having MoS_x photoelectrodeposited for 1 and 10 min as these deposition times provided the highest mean photoresponses (shown in Figure 6b). According to Figure 4a, the Sb 3d spectrum for the bare PT-Sb_2S_3 film displayed photoemission

https://doi.org/10.1021/acsaem.1c03374
ACS Appl. Energy Mater. 2022, 5, 1010−1022

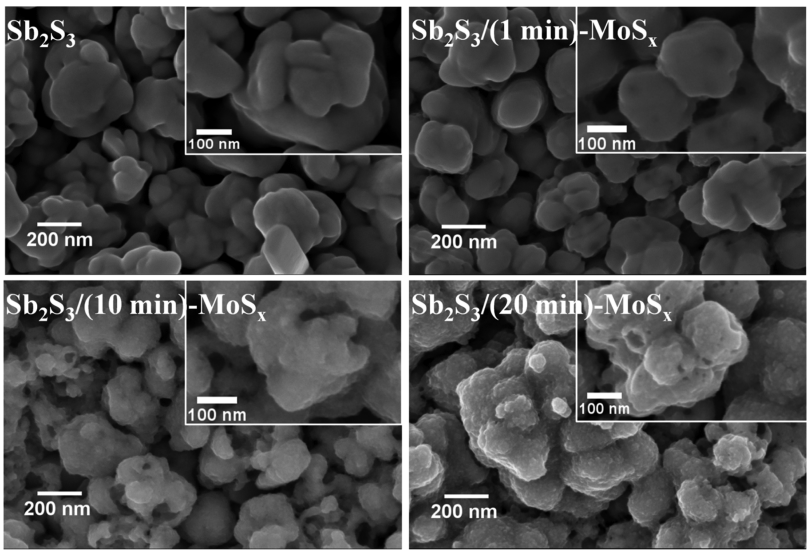

Figure 2. SEM micrographs with a magnification of 150k× for PT-Sb_2S_3 and PT-Sb_2S_3/(1, 10, or 20 min)-MoS_x films.

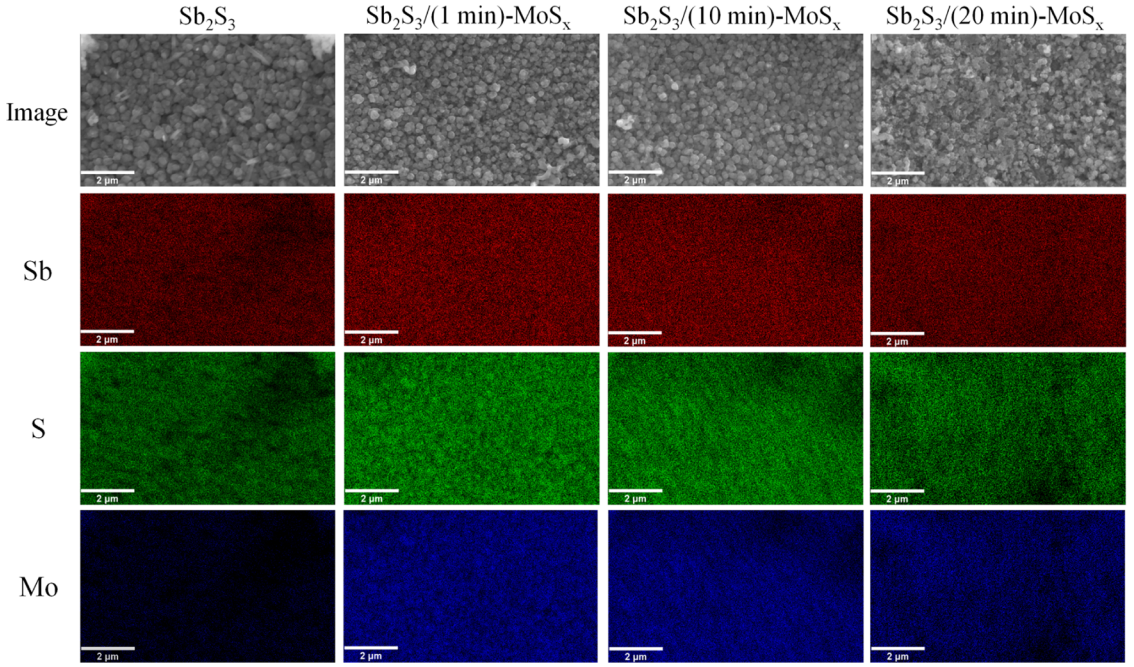

Figure 3. EDS elemental mapping images of Sb, S, and Mo with a magnification of 10k× for PT-Sb_2S_3 and PT-Sb_2S_3/(1, 10, or 20 min)-MoS_x films.

peaks for Sb $3d_{5/2}$ and $3d_{3/2}$ doublets at 531.0 and 540.4 eV, respectively, which were assigned to Sb^{3+} in Sb_2S_3.[34,35] The additional peak at 532.1 eV (O 1s) is probably attributed to adsorbed atmospheric oxygen (O_2, water vapor, etc.) in the S vacancies that can be generated by the ejection of S atoms during the N_2 plasma treatment.[36] For the PT-Sb_2S_3/MoS_x films, the Sb 3d spectra did not show the appearance of new photoemission peaks. Additionally, the Sb $3d_{5/2}$ and $3d_{3/2}$ peaks were not significantly shifted compared to the unmodified film, meaning that the chemical environment of Sb^{3+} species was not modified. Concerning the Mo 3d spectra (cf. Figure 4b), the PT-Sb_2S_3 film presented a photoemission peak at 232.8 eV for the S 2s, which overlaps with the Mo 3d region, and this peak might be associated with the occurrence of nitrogen bonded to sulfur (S−N).[37−39] This result confirms once again what was reported in our previous study that the nitrogen ions from the plasma treatment are very likely to be bonded to sulfur atoms of the Sb_2S_3 film surface.[7] It is worth mentioning that the presence of the superficial S−N group is particularly significant as it is responsible for the hydrophilic behavior of the Sb_2S_3 films once treated under N_2 plasma.[7]

Still, in Figure 4b, the profile of the Mo 3d spectra changed dramatically for the PT-Sb_2S_3/MoS_x films. For both MoS_x photoelectrodeposition times, the spectra showed photoemission peaks of Mo $3d_{5/2}$ at ca. 230.0 eV and Mo $3d_{3/2}$ at ca. 233.2 eV, in which Mo^{4+} species are represented in MoS_2.[40−42] Low-intensity peaks were also noted at approximately 233.0 eV (Mo $3d_{5/2}$) and 236.2 eV (Mo $3d_{3/2}$) assigned to Mo^{6+} present as molybdenum(VI) oxide (MoO_3)[41,43] and/or as molybdenum oxysulfide (MoO_xS_y).[44,45]

https://doi.org/10.1021/acsaem.1c03374
ACS Appl. Energy Mater. 2022, 5, 1010−1022

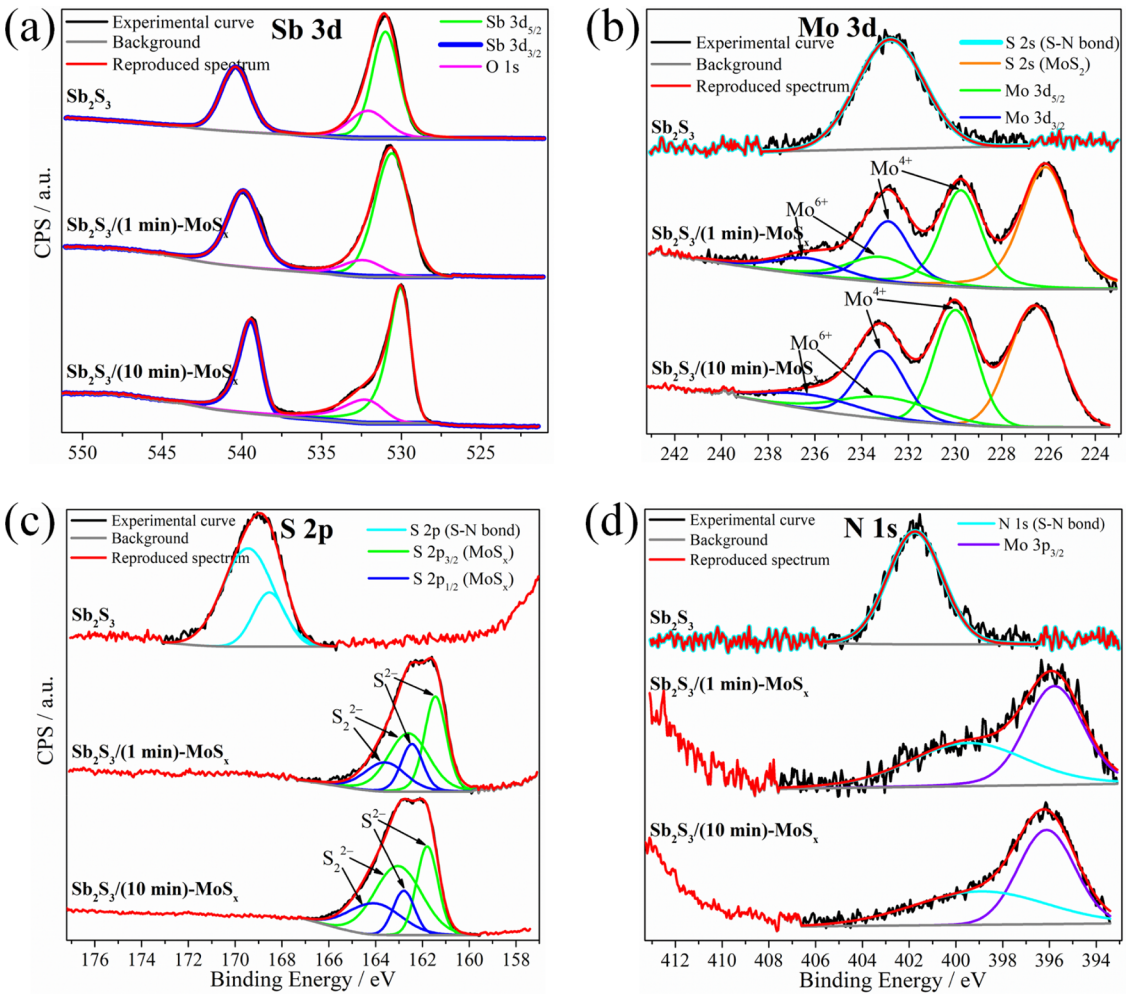

Figure 4. High-resolution XPS spectra of (a) Sb 3d, (b) Mo 3d, (c) S 2p, (d) N 1s core levels for PT-Sb_2S_3 and PT-Sb_2S_3/(1 or 10 min)-MoS_x films.

This MoO_3 or MoO_xS_y may have arisen from the air exposure oxidation process or during the deposition process as the produced OH^- ions (see eq 1) might have facilitated the formation of the MoO_3 or MoO_xS_y compound.[46] The Mo 3d spectra for the films modified with MoS_x also displayed the S 2s peak at ca. 226 eV assigned to MoS_2.[41] Regarding the S 2p spectra (see Figure 4c), the photoemission peaks at 169.5 and 168.5 eV for the PT-Sb_2S_3 film were attributed to the occurrence of the S−N bond.[37,38,47] Such a result backs up what has already been discussed in Figure 4b for the PT-Sb_2S_3 film that the N_2 plasma treatment leads to the formation of the S−N bond on the surface of Sb_2S_3 film. For the PT-Sb_2S_3 films modified with MoS_x, the S 2p spectra did not display the photoemission peaks assigned to the S−N bond. We believe this may be due to the presence of MoS_x over the PT-Sb_2S_3 films that hinders the detection of the S−N bond signal. It was also noted that the S 2p spectra for the PT-Sb_2S_3 films modified with MoS_x presented photoemission peaks at approximately 161.5 eV (S $2p_{3/2}$) and 162.5 eV (S $2p_{1/2}$), which correspond to S^{2-} specie in MoS_x.[46,48] The additional peaks at 162.6 eV (S $2p_{3/2}$) and 163.6 eV (S $2p_{1/2}$) are associated with S_2^{2-} ion in MoS_x.[46,48] According to Ting et al.,[14] the peaks having the lowest binding energies correspond to unsaturated S^{2-} and terminal S_2^{2-}, while the ones with the highest binding energy correspond to the bridging S_2^{2-} and apical S^{2-}. It is worth mentioning that a finer assignment of these different sulfide species at a particular binding energy value is quite difficult to be carried.[14] Nevertheless, among these sulfide species, Ting et al.[14] reported that the bridging S_2^{2-} is the one that provides the most active site in the MoS_x for the occurrence of the HER. Finally, for the N 1s spectra (vide Figure 4d), the photoemission peak at 401.7 eV for the PT-Sb_2S_3 film is assigned quite possibly to the S−N bond.[38,39,49] This serves as additional evidence of what was discussed previously about the formation of the S−N bond during the N_2 plasma treatment. Additionally, the occurrence of the S−N bond was not observed for the untreated film as no signal was displayed in the N 1s spectrum for UT-Sb_2S_3/MoS_x film (cf. Figure S3d). Such a result further verifies that the formation of the S−N group on the Sb_2S_3 films' surface only occurs if the Sb_2S_3 films are treated under N_2 plasma. Still regarding Figure 4d, compared to the bare PT-Sb_2S_3 film, the peak of the S−N bond shifted 2.2 and 2.8 eV toward lower binding energy values for the films having MoS_x photoelectrodeposited for 1 and 10 min, respectively. Such shifting may be an indication that the chemical surroundings of the N atoms were modified by the deposited MoS_x. The N 1s spectra for PT-Sb_2S_3/MoS_x films featured an additional peak at ca. 396 eV, which arises from the Mo $3p_{3/2}$ of the MoS_2 that is

https://doi.org/10.1021/acsaem.1c03374
ACS Appl. Energy Mater. 2022, 5, 1010−1022

overlapped in the N 1s region.[41] The assignment of all photoemission peaks is summarized in Table S2.

Regarding the optical characterization of the films, Tauc plots (cf. Figure 5) were obtained to estimate the optical E_g value for an indirect (allowed) electronic transition. The PT-Sb_2S_3 film presented an estimated optical E_g value of 1.66 ± 0.01 eV, which is in agreement with the one reported in the literature.[4] Estimated optical E_g values of 1.66 ± 0.01, 1.65 ± 0.01, and 1.66 ± 0.01 eV were obtained for the PT-Sb_2S_3 films superficially modified with MoS_x photoelectrodeposited for 1, 10, and 20 min, respectively. As noted, the E_g value for the PT-Sb_2S_3 films was not altered once superficially modified with the MoS_x, meaning that no doping effect occurred in the Sb_2S_3 films during the photoelectrodeposition of the MoS_x. Interestingly, it is reported that MoS_2 has a layer-dependent optical E_g value, that is, bulk MoS_2 features an indirect (allowed) optical E_g of 1.3 eV and a direct (allowed) optical E_g of 1.9 eV once thinned down to a monolayer.[30,50] Nevertheless, in this work, we have not observed the E_g value for the bulk MoS_2 from the Tauc plots in Figure 5. The reason why the E_g of this material was not observed may be related to the existence of amorphous MoS_2.

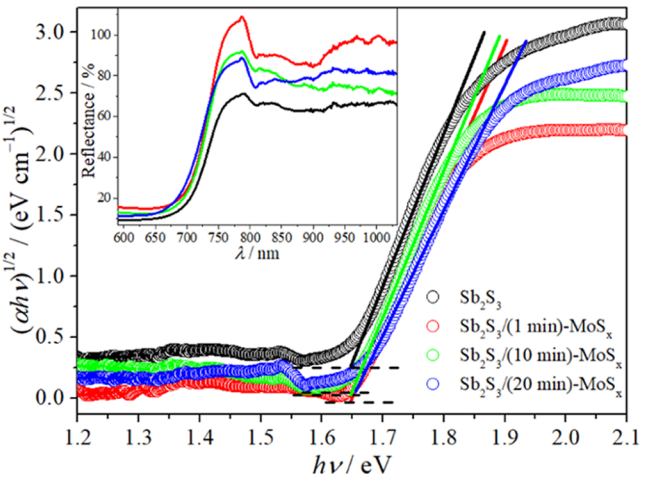

Figure 5. Tauc plots and reflectance spectra (inset) of PT-Sb_2S_3 and PT-Sb_2S_3/(1, 10, or 20 min)-MoS_x films.

It is worth pointing out that the superficial modification of a semiconductor film may result in optical losses, such as reflection, which is deleterious for solar harvesting applications. In this way, we recorded the reflectance spectra of the PT-Sb_2S_3 and the PT-Sb_2S_3/(1, 10, or 20 min)-MoS_x films, and the results are presented as an inset figure in Figure 5. Compared to the bare PT-Sb_2S_3 film, the spectra did not display significant variation of the reflectance values in the visible range (ca. 590−750 nm). There was only an increase of the reflectance values (up to 36%) for the PT-Sb_2S_3/MoS_x films in the near-infrared range (ca. 780−1033 nm) of the spectra. Based on these results, the deposition of MoS_x particles over the PT-Sb_2S_3 films did not result in significant optical losses due to reflection in the absorption range, i.e., visible range, of the semiconductor.

In addition to the physical, chemical, and optical characterization, the PT-Sb_2S_3 films before and after superficially modified with MoS_x were assessed for PEC H_2 generation, as presented hereinafter.

Photoelectrochemical Assessment of the Films. The PEC assessment of the films consisted of initially recording linear sweep voltammograms in the dark and under the solar simulator, which is depicted in Figure 6a.

As seen in Figure 6a, all of the films presented p-type conductivity behavior as a cathodic Δj_{ph} signal was generated. Considering the employed electrolyte, namely, N_2-saturated 1.0 mol L^{-1} H_2SO_4 at its natural pH of 0.6, such cathodic Δj_{ph} response is attributed to the light-driven HER (eqs 2 and 3)[51] on the films.

$$2h\nu \rightarrow 2h^+_{VB} + 2e^-_{CB} \quad (2)$$

$$2H_3O^+_{(aq)} + 2e^-_{CB} \rightarrow H_{2(g)} + 2H_2O_{(l)} \quad (3)$$

in which $h\nu$ is the photon energy to generate e_{CB}^- and h^+_{VB} in the semiconductor.

It was also noted that there was an improvement in PEC H_2 generation as the cathodic Δj_{ph} responses were higher in the entire range of potentials for the PT-Sb_2S_3/(1, 10, or 20 min)-MoS_x films in comparison to the bare PT-Sb_2S_3 film. In terms

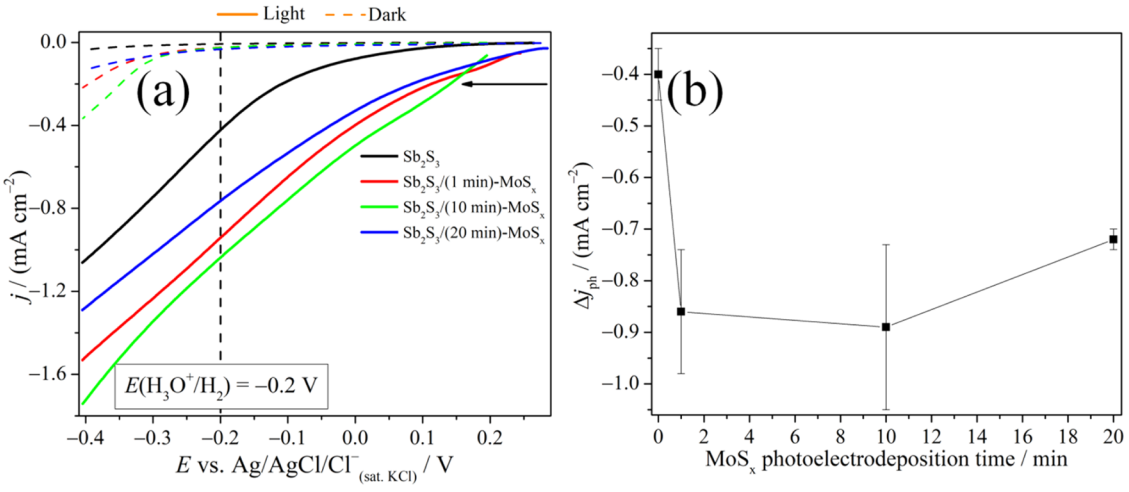

Figure 6. (a) Linear sweep voltammograms at a scan rate of 50 mV s^{-1} in the dark and under solar light simulator (AM1.5G and 100 mW cm^{-2}) and (b) mean Δj_{ph} values at −0.2 V vs Ag/AgCl/$Cl_{(sat.\ KCl)}^-$ for PT-Sb_2S_3 and PT-Sb_2S_3/(1, 10, or 20 min)-MoS_x films. The electrolyte was a N_2-saturated solution of 1.0 mol L^{-1} H_2SO_4 at pH 0.6.

https://doi.org/10.1021/acsaem.1c03374
ACS Appl. Energy Mater. 2022, 5, 1010−1022

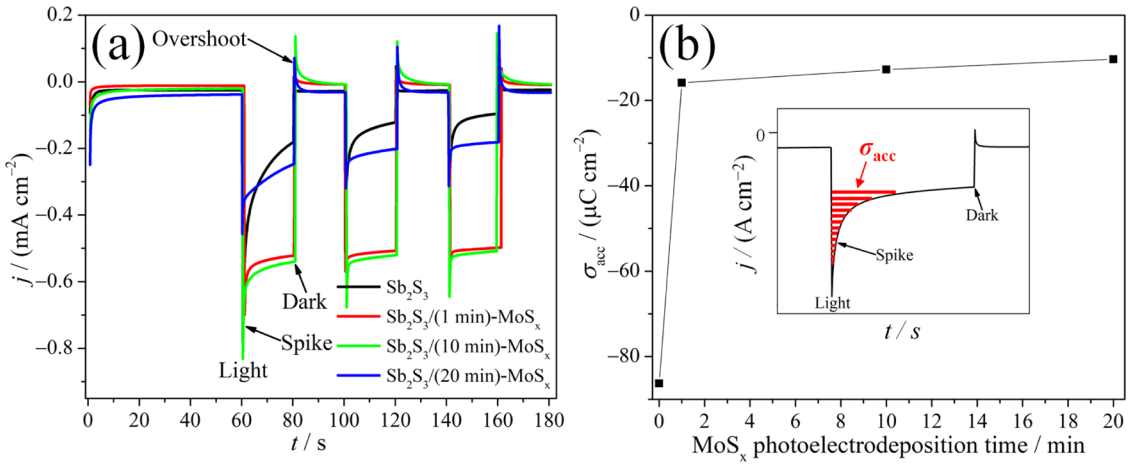

Figure 7. (a) Transient Δj_{ph} responses at −0.2 V vs Ag/AgCl/$Cl_{(sat.\ KCl)}^-$ and under a chopped solar light simulator (AM1.5G and 100 mW cm^{-2}) and (b) σ_{acc} values at −0.2 V vs Ag/AgCl/$Cl_{(sat.\ KCl)}^-$ for PT-Sb_2S_3 and PT-Sb_2S_3/(1, 10, or 20 min)-MoS_x films. The electrolyte was a N_2-saturated solution of 1.0 mol L^{-1} H_2SO_4 at pH 0.6.

of Δj_{ph} values at −0.2 V (corresponds to 0 V vs RHE), as summarized in Figure 6b, the PT-Sb_2S_3 films having MoS_x photoelectrodeposited for 1, 10, and 20 min presented values of −0.86 ± 0.12, −0.89 ± 0.16, and −0.72 ± 0.02 mA cm^{-2}, respectively. These values indicated that there was not a dependency of the MoS_x photoelectrodeposition time with the photoelectroactivity of the PT-Sb_2S_3/MoS_x films. However, the presence of the MoS_x over the PT-Sb_2S_3 films provided an approximately 2-fold increase in the cathode Δj_{ph} response compared to the bare PT-Sb_2S_3 film (−0.40 ± 0.05 mA cm^{-2}). It was also noticed from Figure 6a that modifying the PT-Sb_2S_3 film surface with MoS_x resulted in shifting the E_{on} in ca. 100 mV toward less negative values, which is due to the catalytic activity of MoS_x for the HER.[52] This catalytic behavior is probably associated with the presence of S_2^{2-} species[14] in MoS_x, as observed in the S 2p XPS spectra (see Figure 4c). Additionally, the E_{on} shift toward less negative values stands advantageously as it facilitates the occurrence of the HER by diminishing the energy input or the overpotential of the system (PT-Sb_2S_3/MoS_x films).

Further PEC analysis of the bare PT-Sb_2S_3 and the PT-Sb_2S_3/(1, 10, or 20 min)-MoS_x films were performed by means of the transients' Δj_{ph} measurements at −0.2 V and under chopped illumination. As can be noted in Figure 7a, under illumination, the transients' Δj_{ph} profile for all of the films featured a sharp cathodic Δj_{ph} rise followed by an exponential decay, known as a spike. The existence of spikes is associated with the occurrence of the electron−hole recombination process at the semiconductor surface,[53] as observed for a variety of semiconductor materials.[53−56] Once the illumination was interrupted, an anodic current density overshoot was observed, which is attributed to the recombination of holes with electrons accumulated or trapped on surface states.[57] Such a phenomenon is known as back-electron−hole recombination because there is a backflow of holes from the semiconductor's bulk toward its surface to recombine with the accumulated electrons.[53]

Aiming at a quantitative analysis of the transients, the spike curves in Figure 7a were integrated as it provides the accumulated charge density (σ_{acc}), which is proportional to the number of negative charges (electrons) accumulated at the surface.[54] It is interesting to point out that the calculated σ_{acc} values can also be represented by the area of the spike (cf. the inset of Figure 7b). For this study, the σ_{acc} value of the last Δj_{ph} transient for bare PT-Sb_2S_3 and PT-Sb_2S_3/(1, 10, or 20 min)-MoS_x films was calculated, and the results are exhibited in Figure 7b. The σ_{acc} value slightly changed over the photoelectrodeposition time of MoS_x on PT-Sb_2S_3, and similar trending was observed for the Δj_{ph} response (see Figure 6b). Additionally, the σ_{acc} value dramatically diminished by a factor of 8.4 for PT-Sb_2S_3/MoS_x films in comparison with bare PT-Sb_2S_3 film (from −86.3 to −10.3 μC cm^{-2}). This result indicates that a certain amount of photogenerated electrons may have been accumulated on the surface of the PT-Sb_2S_3 films as the reduced σ_{acc} values only occurred for PT-Sb_2S_3 films superficially modified with MoS_x. No doping occurred during the superficial modification of PT-Sb_2S_3 films with MoS_x as there was neither variation of the E_g values (vide Figure 5) or shifting of the diffraction peaks (see Figure 1), and this comes as additional evidence that the photogenerated electrons are accumulated on the surface of the PT-Sb_2S_3 films. Such accumulation might be occurring in defective energy levels or surface defects, which may eventually act as recombination centers.[58,59] As recently reported,[58−60] the surface defects may be assigned to electron/hole trap sites, dangling bond, mismatching lattice, interdiffusion, antisite defects, etc., which are probably located above the valence band of Sb_2S_3. The accumulation of the photogenerated electrons may have also taken place in sulfur vacancies of PT-Sb_2S_3, which were probably generated during the N_2 plasma treatment. These vacancies might have been formed from the ejection of sulfur atoms that occurs due to the collision of the N_2 plasma species against the surface of the Sb_2S_3 films. Ejection of atoms (also known as the etching effect) can occur in the event that species from plasma collide against films' surface with high kinetic energy.[61] Formation of sulfur vacancies from plasma treatment has been reported for several sulfide-based compounds.[36,62,63] Based on all of these, the observed reduction of σ_{acc} values for the PT-Sb_2S_3/MoS_x films might be due to the extraction of the trapped electrons from the PT-Sb_2S_3 film surface by the MoS_x co-catalyst. Extraction of carriers from the semiconductor's surface by a co-catalyst was also observed for hematite films superficially modified with cobalt.[54] Additionally, the observed decrease of σ_{acc} values in the surface implies a smaller probability of the electron−hole recombination process for the PT-Sb_2S_3/MoS_x films, which

https://doi.org/10.1021/acsaem.1c03374
ACS Appl. Energy Mater. 2022, 5, 1010−1022

explains their photoelectroactivity enhancement and the E_{on} shifting toward less negative values (see Figure 6).

Seeking to gain further understanding of the photoelectroresponse enhancement of the PT-Sb_2S_3/MoS_x system, Mott−Schottky plots were obtained and are shown in Figure 8

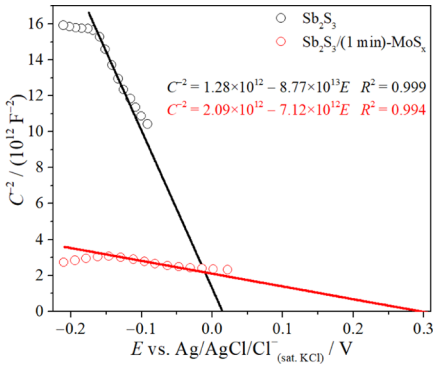

Figure 8. Mott−Schottky plots for PT-Sb_2S_3 and PT-Sb_2S_3/(1 min)-MoS_x films. The electrolyte was an N_2-saturated solution of 1.0 mol L^{-1} H_2SO_4 at pH 0.6.

for the PT-Sb_2S_3 film before and after superficially modified with MoS_x photoelectrodeposited for 1 min. Only the 1 min photoelectrodeposition time of MoS_x was chosen as the other photoelectrodeposition times did not provide significant photoelectroresponse enhancement of the PT-Sb_2S_3/MoS_x system (see Figure 6b). The Mott−Schottky curves in Figure 8 presented a negative slope for both films, meaning that these materials are p-type semiconductors as previously discussed at the beginning of Figure 6a. The Mott−Schottky plots also provided the means to estimate E_{fb} via eq 4.[64,65]

$$E_{fb}\ (\text{vs Ag/AgCl/Cl}^-_{(\text{sat. KCl})}) \approx -\frac{\text{intercept}}{\text{slope}} - \frac{kT}{e} \qquad (4)$$

in which k is the Boltzmann constant (1.38×10^{-23} J K^{-1}), T is the absolute temperature (298.15 K), e is the elementary charge (1.60×10^{-19} C), and the slope and intercept values were obtained from the linear equations in Figure 8.

Employing the parameters of the linear equation (slope and intercept) from Figure 8 in eq 4, it provided E_{fb} values of −0.01 and 0.27 V for bare PT-Sb_2S_3 and PT-Sb_2S_3/(1 min)-MoS_x films, respectively. Compared to the bare PT-Sb_2S_3 film, E_{fb} shifted 280 mV toward less negative values for the PT-Sb_2S_3/(1 min)-MoS_x film, which is linked to the co-catalytic behavior of the MoS_x for the HER as already observed in the linear sweep voltammograms of Figure 6a.

Finally, additional understanding about the photoelectroresponse enhancement for the PT-Sb_2S_3/(1 min)-MoS_x system was achieved by the EIS analyses, which were obtained under illumination and polarized at −0.2 V (cf. Figure 9a). For the sake of comparison, this experiment was also performed for the bare PT-Sb_2S_3 film. According to Figure 9a, the complex-plane diagram of both films displayed at least one semicircle, and this might be ascribed to the occurrence of the interfacial charge transfer processes. To fully unravel the underlying photophysical and electrochemical processes, the diagrams in Figure 9a were carefully fitted to an electrical circuit model, which is displayed as an inset in Figure 9a. The employed circuit was composed of a solution resistance (R_s) connected in series with two RC components ($R_{ct,sc}$/CPE_{sc} and $R_{ct,d}$/CPE_d); these components in the Bode diagrams (cf. Figure 9b) are associated with the asymmetrical broad peak for both films. Keeping in mind that the electronic processes in the semiconductor's bulk are usually faster than the charge transfer processes of ion diffusion in solution, the high-frequency domain is assigned to processes occurring in the semiconductor, which is represented by the $R_{ct,sc}$ and CPE_{sc} components.[66] The former and latter components are the charge transfer resistance and the capacitance in the space charge of the semiconductor, respectively. The low-frequency domain is designated to the charge transfer event at the semiconductor|electrolyte interface. This phenomenon is represented by the $R_{ct,d}$ and CPE_d components which corresponded to the charge transfer resistance and the double-layer capacitance at the semiconductor|electrolyte

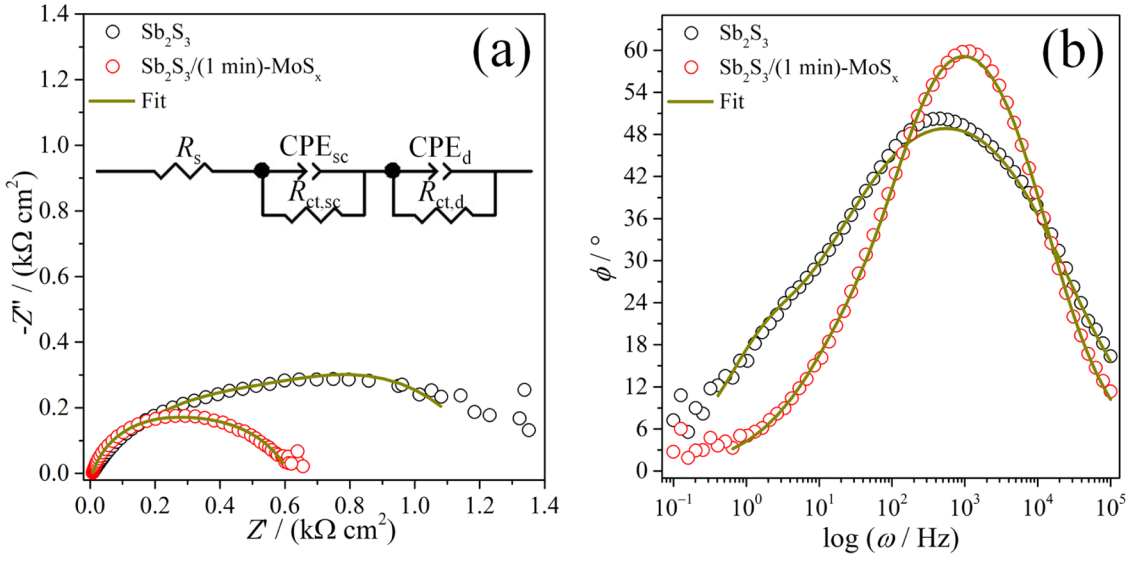

Figure 9. (a) Complex-plane impedance diagrams and (b) Bode diagrams at −0.2 V vs $Ag/AgCl/Cl^-_{(sat.\ KCl)}$ and under solar light simulator (AM1.5G and 100 mW cm^{-2}) for PT-Sb_2S_3 and PT-Sb_2S_3/(1 min)-MoS_x films. The electrolyte was a N_2-saturated solution of 1.0 mol L^{-1} H_2SO_4 at pH 0.6.

https://doi.org/10.1021/acsaem.1c03374
ACS Appl. Energy Mater. 2022, 5, 1010−1022

Table 1. Resistance and Capacitance Values of the Electrical Circuit Model Used to Fit the Complex-Plane Impedance Diagrams

sample	R_s (Ω cm^2)	$R_{ct,sc}$ (Ω cm^2)	$R_{ct,d}$ (Ω cm^2)	Q_{sc}[a] (Ω^{-1} cm^{-2} $s^{\alpha f,sc}$)	Q_d[a] (Ω^{-1} cm^{-2} $s^{\alpha f,d}$)	C_{sc}[b] (μF cm^{-2})	C_d[b] (μF cm^{-2})
PT-Sb_2S_3	6.8	499.1	714.6	3.75×10^{-4} ($\alpha_{f,sc} = 0.86$)	7.87×10^{-5} ($\alpha_{f,d} = 0.63$)	285.5	14.5
PT-Sb_2S_3/(1 min)-MoS_x	7.3	223.5	381.4	1.55×10^{-5} ($\alpha_{f,sc} = 0.86$)	9.46×10^{-5} ($\alpha_{f,d} = 0.71$)	6.2	24.4

[a]Q_{sc} and Q_d are the pseudocapacitance in the space charge of semiconductor and the double layer at the semiconductor|electrolyte interface, respectively, while α_f is their corresponding CPE exponent. [b]The real capacitance of the space charge (C_{sc}) of semiconductor and the real capacitance of the double layer (C_d) at the semiconductor|electrolyte interface were calculated from eq 5.

Scheme 2. Schematic Representation of the MoS_x Co-catalyst Effect on the Photoelectroactivity of PT-Sb_2S_3 Films for PEC H_2 Generation[a]

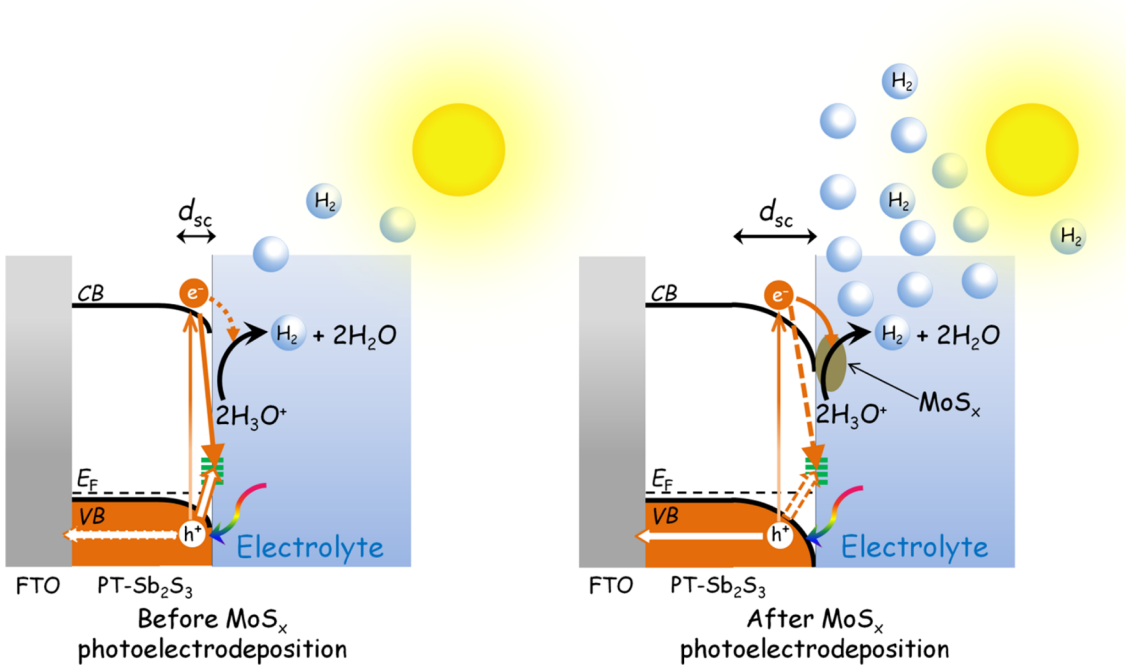

[a]The solid and dotted orange lines denote the majority and minority events, respectively. Band diagram not drawn to scale.

interface, respectively.[66] For a better fitting of the data, a constant phase element (CPE), i.e., a non-ideal capacitor, was used. The real values of the capacitance density (C) were obtained from the CPE parameter (Q), also known as CPE-T, and R_{ct}, as shown in eq 5.[67]

$$C = \frac{(QR_{ct})^{1/\alpha_f}}{R_{ct}} \tag{5}$$

in which Q is the pseudocapacitance and α_f is the CPE exponent, also known as CPE-P, which can take a value between 0 and 1. The CPE behaves like an ideal capacitor for α_f being equal to 1.

The calculated C values as well as the fitted data of each element in the circuit are summarized in Table 1. The percentage error values from the fitting for each element in the circuit are listed in Table S3.

Given the data in Table 1, there was a 2.2-fold decrease of the $R_{ct,sc}$ value for the PT-Sb_2S_3/(1 min)-MoS_x film in comparison with the PT-Sb_2S_3 film. The decreased $R_{ct,sc}$ for the superficially modified film stands advantageously as it favors a faster transfer of the e^-_{CB} across the depletion layer and/or the bulk region of the PT-Sb_2S_3 film.[68] Compared to the PT-Sb_2S_3 film, there was also a 1.9-fold decrease of the $R_{ct,d}$ value for the PT-Sb_2S_3/(1 min)-MoS_x film. Such a decrease was also attributed to a faster transfer of e^-_{CB} at the PT-Sb_2S_3/(1 min)-MoS_x|electrolyte interface.[68,69] Collating these results with the Δj_{ph} responses in Figure 6, the improved photoresponse for the PT-Sb_2S_3/MoS_x films is linked to the reduced values of $R_{ct,sc}$ and R_d that facilitates carrier transfer to the electrolyte. Another implication was the minimization of the electron−hole recombination process due to the facilitation of the interfacial carrier transfer as noted from the reduction of σ_{acc} values for the PT-Sb_2S_3/MoS_x films in Figure 7b.

Concerning the capacitance density values in Table 1, C_{sc} substantially decreased 46-fold for the PT-Sb_2S_3/(1 min)-MoS_x compared to the PT-Sb_2S_3 film. This decrease of C_{sc} can be a result of increasing the thickness of the space charge (d_{sc}) layer under depletion conditions, which is defined by eq 6.[70]

$$d_{sc} = \frac{\varepsilon_r \varepsilon_0}{C_{sc}} \tag{6}$$

in which ε_r is the relative permittivity of Sb_2S_3 and ε_0 is the permittivity of vacuum.

Increasing d_{sc} can lead to an enlargement of the (quasi-)Fermi level gradient in the space charge region and consequently enhancement in carrier separation as well as an increase in the photoelectroactivity as seen in Figure 6. The decrease of C_{sc} for the PT-Sb_2S_3/(1 min)-MoS_x film can also

https://doi.org/10.1021/acsaem.1c03374
ACS Appl. Energy Mater. 2022, 5, 1010−1022

be understood by the reduction of electrons accumulated in surface traps (see the discussion of Figure 7b). Still regarding the capacitance density values in Table 1, one can also note that C_d slightly increased for PT-Sb_2S_3/(1 min)-MoS_x in comparison with the bare PT-Sb_2S_3 film. Bearing in mind that C_d is proportional to the surface area of the solidlelectrolyte interface,[69] the slight increase of C_d might be associated with the increase of the surface area of the PT-Sb_2S_3 film by the presence of the nanoparticles of MoS_x. This probably increased the surface area of the PT-Sb_2S_3/(1 min)-MoS_x film, which may have also contributed to the enhancement of its photoresponse for the HER.

Building on all of these findings presented herein, we believe that the role of MoS_x on the photoelectroactivity improvement of the PT-Sb_2S_3 films is due to the minimization of the superficial electron−hole recombination process by the collection of a photogenerated electron trapped in the surface of the PT-Sb_2S_3 films. Additionally, the presence of MoS_x enabled minimization of recombination process and consequently improvement of PEC H_2 generation by reducing resistance as well as an increase of d_{sc}. The contribution of MoS_x on the photoelectroactivity enhancement of the PT-Sb_2S_3 films is summarized in Scheme 2. It is worth clarifying that we have not employed E_g values and electrochemical data to construct the band diagram in Scheme 2, which only served the purpose of better explaining the improvement of H_2 generation on the Sb_2S_3/MoS_x system.

CONCLUSIONS

Herein, we have successfully improved the photoelectroactivity of PT-Sb_2S_3 films for the HER by depositing the earth-abundant MoS_x co-catalyst onto their surface via photoelectrodeposition. Albeit the photoresponse of PT-Sb_2S_3/MoS_x films did not significantly vary over the MoS_x photoelectrodeposition time, the presence of the MoS_x nanoparticles enabled a 2-fold increase of the cathodic Δj_{ph} response. Based on a thorough analysis of the transient Δj_{ph} responses, the enhanced photoelectroactivity was assigned to a smaller probability of the electron−hole recombination process for the PT-Sb_2S_3/MoS_x films, as noted from the substantial reduction of the σ_{acc} values. The reduced occurrence of the recombination process is probably linked to the MoS_x co-catalyst that may have extracted the photogenerated electrons trapped in the defective energy levels (i.e., recombination centers) of the surface of the PT-Sb_2S_3 films. The minimization of carriers recombination was also verified from the decrease of the R_{ct} values by approximately 2-fold for the PT-Sb_2S_3/MoS_x films, as observed from the EIS results. Additionally, the PT-Sb_2S_3/MoS_x featured an increase of d_{sc}, meaning improvement of carrier separation or minimized recombination process due to the enlarged gradient of the (quasi-)Fermi level in the space charge region of the PT-Sb_2S_3 films. The presence of MoS_x nanoparticles on the PT-Sb_2S_3 films also resulted in the shift of E_{on} toward less negative potential values, which indicated that the combination of MoS_x with the PT-Sb_2S_3 films co-catalyzed the light-driven HER. Acting in the same manner as the E_{on} shifting behavior,E_{fb} from the Mott−Schottky plots shifted to less negative values for the PT-Sb_2S_3/MoS_x, thus substantiating the role of MoS_x as a co-catalyst of PT-Sb_2S_3 films for the HER. In view of these results, our work has achieved superlative performance of the PT-Sb_2S_3/MoS_x films for PEC H_2 generation. Additionally, we have employed electrodeposition, a low-cost methodology, to obtain the PT-Sb_2S_3/MoS_x system, which is fully composed of earth-abundant and low-toxicity elements. All of these features make our system, i.e., PT-Sb_2S_3/MoS_x, a highly promising candidate for a large-scale application of PEC cells in the near future.

ASSOCIATED CONTENT

Supporting Information

The Supporting Information is available free of charge at https://pubs.acs.org/doi/10.1021/acsaem.1c03374.

Cyclic voltammograms for MoS_x photoelectrodeposition; linear sweep voltammograms in the dark and under illumination for UT-Sb_2S_3/MoS_x and PT-Sb_2S_3/MoS_x films; high-resolution XPS spectra for UT-Sb_2S_3/MoS_x film; particle size distribution histograms for PT-Sb_2S_3 and PT-Sb_2S_3/(1, 10, or 20 min)-MoS_x films; EDS spectra and EDS quantification plots for PT-Sb_2S_3 and PT-Sb_2S_3/(1, 10, or 20 min)-MoS_x films; atomic percentage of Sb and S; binding energy assignment; and percentage error values for each circuit element to fit the complex-plane impedance diagrams (PDF)

AUTHOR INFORMATION

Corresponding Author

Lucia H. Mascaro − *Departamento de Química, Universidade Federal de São Carlos, São Carlos, São Paulo 13565-905, Brazil;* orcid.org/0000-0001-6908-1097; Email: lmascaro@ufscar.br

Authors

Moisés A. de Araújo − *Departamento de Química, Universidade Federal de São Carlos, São Carlos, São Paulo 13565-905, Brazil;* Present Address: Instituto de Química de São Carlos, Universidade de São Paulo, Avenida Trabalhador Sancarlense, 400, São Carlos, São Paulo 13566-590, Brazil

Magno B. Costa − *Departamento de Química, Universidade Federal de São Carlos, São Carlos, São Paulo 13565-905, Brazil*

Complete contact information is available at: https://pubs.acs.org/10.1021/acsaem.1c03374

Author Contributions

M.A.d.A. contributed to the conceptualization, methodology, validation, formal analysis, investigation, data curation, and writing—original draft. M.B.C. involved in the conceptualization, investigation, and writing—review and editing. L.H.M. contributed to resources, writing—review and editing, and supervision.

Notes

The authors declare no competing financial interest.

ACKNOWLEDGMENTS

This work has emanated from research conducted with the financial support of the São Paulo Research Foundation (FAPESP) under the grants: #2016/12681-0 (M.A.d.A.), #2013/07296-2 (CEPID/CDMF), #2017/21365-8 (M.B.C.), and #2017/11986-5 (FAPESP/SHELL). The authors also gratefully acknowledge Prof. Valmor R. Mastelaro who kindly performed the XPS measurements.

REFERENCES

(1) Lehman, C.; Bensaude-Vincent, B. Public Demonstrations of Chemistry in Eighteenth Century France. *Sci. Educ.* **2007**, *16*, 573−583.

(2) Chang, H. *Is Water H_2O? Evidence, Realism and Pluralism*; Springer, 2012; Vol. *293*.

(3) Ding, Q.; Song, B.; Xu, P.; Jin, S. Efficient Electrocatalytic and Photoelectrochemical Hydrogen Generation Using MoS_2 and Related Compounds. *Chem* **2016**, *1*, 699−726.

(4) Lei, H.; Chen, J.; Tan, Z.; Fang, G. Review of Recent Progress in Antimony Chalcogenide-Based Solar Cells: Materials and Device. *Sol. RRL* **2019**, *3*, No. 1900026.

(5) Wang, Y.-C.; Zeng, Y.-Y.; Li, L.-H.; Qin, C.; Wang, Y.-W.; Lou, Z.-R.; Liu, F.-Y.; Ye, Z.-Z.; Zhu, L.-P. A Stable and Efficient Photocathode Using Sb_2S_3 Absorber in Near-Neutral Electrolyte for Water Splitting. *ACS Appl. Energy Mater.* **2020**, *3*, 6188−6194.

(6) Medina-Montes, M. I.; Montiel-González, Z.; Paraguay-Delgado, F.; Mathews, N. R.; Mathew, X. Structural, Morphological and Spectroscopic Ellipsometry Studies on Sputter Deposited Sb_2S_3 Thin Films. *J. Mater. Sci. Mater. Electron.* **2016**, *27*, 9710−9719.

(7) de Araújo, M. A.; Mascaro, L. H. Plasma Treatment: a Novel Approach to Improve the Photoelectroactivity of Sb_2S_3 Thin Films to Water Splitting. *ChemElectroChem* **2020**, *7*, 2325−2329.

(8) Darga, A.; Mencaraglia, D.; Longeaud, C.; Savenije, T. J.; O'Regan, B.; Bourdais, S.; Muto, T.; Delatouche, B.; Dennler, G. On Charge Carrier Recombination in Sb_2S_3 and its Implication for the Performance of Solar Cells. *J. Phys. Chem. C* **2013**, *117*, 20525−20530.

(9) DeAngelis, A. D.; Kemp, K. C.; Gaillard, N.; Kim, K. S. Antimony(III) Sulfide Thin Films as a Photoanode Material in Photocatalytic Water Splitting. *ACS Appl. Mater. Interfaces* **2016**, *8*, 8445−8451.

(10) de Araújo, M. A.; Lucas, F. W. S.; Mascaro, L. H. Effect of the Electrodeposition Potential on the Photoelectroactivity of the SnS/Sb_2S_3 Thin Films. *J. Solid State Electrochem.* **2020**, *24*, 389−399.

(11) Lu, X.; Liu, Z. Efficient all p-Type Heterojunction Photocathodes for Photoelectrochemical Water Splitting. *Dalton Trans.* **2017**, *46*, 7351−7360.

(12) Li, H.; Tsai, C.; Koh, A. L.; Cai, L.; Contryman, A. W.; Fragapane, A. H.; Zhao, J.; Han, H. S.; Manoharan, H. C.; Abild-Pedersen, F.; Nørskov, J. K.; Zheng, X. Activating and Optimizing MoS_2 Basal Planes for Hydrogen Evolution through the Formation of Strained Sulphur Vacancies. *Nat. Mater.* **2016**, *15*, 48−53.

(13) Kang, D.; Kim, T. W.; Kubota, S. R.; Cardiel, A. C.; Cha, H. G.; Choi, K.-S. Electrochemical Synthesis of Photoelectrodes and Catalysts for Use in Solar Water Splitting. *Chem. Rev.* **2015**, *115*, 12839−12887.

(14) Ting, L. R. L.; Deng, Y.; Ma, L.; Zhang, Y.-J.; Peterson, A. A.; Yeo, B. S. Catalytic Activities of Sulfur Atoms in Amorphous Molybdenum Sulfide for the Electrochemical Hydrogen Evolution Reaction. *ACS Catal.* **2016**, *6*, 861−867.

(15) Tran, P. D.; Pramana, S. S.; Kale, V. S.; Nguyen, M.; Chiam, S. Y.; Batabyal, S. K.; Wong, L. H.; Barber, J.; Loo, J. Novel Assembly of an MoS_2 Electrocatalyst onto a Silicon Nanowire Array Electrode to Construct a Photocathode Composed of Elements Abundant on the Earth for Hydrogen Generation. *Chem.—Eur. J.* **2012**, *18*, 13994−13999.

(16) Prabhakar, R. R.; Septina, W.; Siol, S.; Moehl, T.; Wick-Joliat, R.; Tilley, S. D. Photocorrosion-Resistant Sb_2Se_3 Photocathodes with Earth Abundant MoS_x Hydrogen Evolution Catalyst. *J. Mater. Chem. A* **2017**, *5*, 23139−23145.

(17) Seabold, J. A.; Choi, K.-S. Efficient and Stable Photo-Oxidation of Water by a Bismuth Vanadate Photoanode Coupled with an Iron Oxyhydroxide Oxygen Evolution Catalyst. *J. Am. Chem. Soc.* **2012**, *134*, 2186−2192.

(18) Zhang, Z.; Zhao, J.; Xu, M.; Wang, H.; Gong, Y.; Xu, J. Facile Synthesis of Sb_2S_3/MoS_2 Heterostructure as Anode Material for Sodium-Ion Batteries. *Nanotechnology* **2018**, *29*, No. 335401.

(19) Li, P.; Jeong, J. Y.; Jin, B.; Zhang, K.; Park, J. H. Large and reversible sodium storage through interlaced reaction design. *Energy Storage Mater.* **2020**, *25*, 687−694.

(20) Cai, Q.; Liu, Z.; Han, C.; Tong, Z.; Ma, C. $CuInS_2$/Sb_2S_3 Heterostructure Modified with Noble Metal Co-Catalyst for Efficient Photoelectrochemical Water Splitting. *J. Alloys Compd.* **2019**, *795*, 319−326.

(21) Siegrist, T. Crystallographica - A Software Toolkit for Crystallography. *J. Appl. Crystallogr.* **1997**, *30*, 418−419.

(22) Fairley, N.; Fernandez, V.; Richard-Plouet, M.; Guillot-Deudon, C.; Walton, J.; Smith, E.; Flahaut, D.; Greiner, M.; Biesinger, M.; Tougaard, S.; Morgan, D.; Baltrusaitis, J. Systematic and Collaborative Approach to Problem Solving Using X-Ray Photoelectron Spectroscopy. *Appl. Surf. Sci. Adv.* **2021**, *5*, No. 100112.

(23) Du, H.; Yang, C.; Pu, W.; Zhao, H.; Gong, J. Highly Active Sb_2S_3-attached Mo−WO_3 Composite Film for Enhanced Photoelectrocatalytic Water Splitting at Extremely low Input Light Energy. *ACS Sustainable Chem. Eng.* **2019**, *7*, 9172−9181.

(24) Moulder, J. F.; Stickle, W. F.; Sobol, P. E.; Bomben, K. D. *Handbook of X-ray Photoelectron Spectroscopy*; PerkinElmer Corporation, 1992.

(25) Paunovic, M.; Schlesinger, M. *Fundamentals of Electrochemical Deposition*; John Wiley & Sons, Inc., 2006.

(26) Bayliss, P.; Nowacki, W. Refinement of the Crystal Structure of Stibinite, Sb_2S_3. *Z. Kristallogr.—Cryst. Mater.* **1972**, *135*, 308−315.

(27) McMurdie, H. F.; Morris, M. C.; Evans, E. H.; Paretzkin, B.; Wong-Ng, W.; Hubbard, C. R. Standard X-Ray Diffraction Powder Patterns from the JCPDS Research Associateship. *Powder Diffr.* **1986**, *1*, 265−275.

(28) Jellinek, F.; Brauer, G.; Müller, H. Molybdenum and Niobium Sulphides. *Nature* **1960**, *185*, 376−377.

(29) McCarthy, G. J.; Welton, J. M. X-Ray Diffraction Data for SnO_2. An Illustration of the New Powder Data Evaluation Methods. *Powder Diffr.* **1989**, *4*, 156−159.

(30) Han, B.; Hu, Y. H. MoS_2 as a Co-Catalyst for Photocatalytic Hydrogen Production from Water. *Energy Sci. Eng.* **2016**, *4*, 285−304.

(31) Medina, M.; Corradini, P. G.; Mascaro, L. H. Facile One-Step Electrodeposition Fabrication of Amorphous MoS_2 Catalysts in Titanium for Hydrogen Evolution Reaction. *J. Braz. Chem. Soc.* **2019**, *30*, 2210−2218.

(32) Liu, C.; Liu, T.; Li, Y.; Zhao, Z.; Zhou, D.; Li, W.; Zhao, Y.; Yang, H.; Sun, L.; Li, F.; Li, Z. A Dendritic Sb_2Se_3/In_2S_3 Heterojunction Nanorod Array Photocathode Decorated with a MoS_x Catalyst for Efficient Solar Hydrogen Evolution. *J. Mater. Chem. A* **2020**, *8*, 23385−23394.

(33) Grieken, R. E. V.; Markowicz, A. A. *Handbook of X-ray Spectrometry*; Marcel Dekker, Inc., 2002.

(34) Morgan, W. E.; Stec, W. J.; Wazer, J. R. V. Inner-Orbital Binding-Energy Shifts of Antimony and Bismuth Compounds. *Inorg. Chem.* **1973**, *12*, 953−955.

(35) Zakaznova-Herzog, V. P.; Harmer, S. L.; Nesbitt, H. W.; Bancroft, G. M.; Flemming, R.; Pratt, A. R. High Resolution XPS Study of the Large-Band-Gap Semiconductor Stibnite (Sb_2S_3): Structural Contributions and Surface Reconstruction. *Surf. Sci.* **2006**, *600*, 348−356.

(36) Chow, P. K.; Singh, E.; Viana, B. C.; Gao, J.; Luo, J.; Li, J.; Lin, Z.; Elías, A. L.; Shi, Y.; Wang, Z.; Terrones, M.; Koratkar, N. Wetting of Mono and Few-Layered WS_2 and MoS_2 Films Supported on Si/SiO_2 Substrates. *ACS Nano* **2015**, *9*, 3023−3031.

(37) Mengel, P.; Grant, P. M.; Rudge, W. E.; Schechtman, B. H.; Rice, D. W. X-Ray-Photoelectron-Spectroscopy Determination of the Valence Band Structure of Polymeric Sulfur Nitride, $(SN)_x$. *Phys. Rev. Lett.* **1975**, *35*, 1803−1806.

(38) Brant, P.; Weber, D. C.; Ewing, C. T.; Carter, F. L.; Hashmall, J. A. The Application of Gas Phase and Solid State X-Ray Photoelectron Spectroscopy to the Investigation of Derivatives Containing the Repeating SN Unit. *Synth. Met.* **1980**, *1*, 161−173.

https://doi.org/10.1021/acsaem.1c03374
ACS Appl. Energy Mater. 2022, 5, 1010−1022

(39) Sharma, J.; Downs, D. S.; Iqbal, Z.; Owens, F. J. X-Ray Photoelectron Spectroscopy of S_2N_2 and the Solid State Polymerization of S_2N_2 to Metallic $(SN)_x$. *J. Chem. Phys.* **1977**, *67*, 3045.
(40) Stevens, G. C.; Edmonds, T. Electron Spectroscopy for Chemical Analysis Spectra of Molybdenum Sulfides. *J. Catal.* **1975**, *37*, 544−547.
(41) Ganta, D.; Sinha, S.; Haasch, R. T. 2-D Material Molybdenum Disulfide Analyzed by XPS. *Surf. Sci. Spectra* **2014**, *21*, 19.
(42) Wang, X.; Cormier, C. R.; Khosravi, A.; Smyth, C. M.; Shallenberger, J. R.; Addou, R.; Wallace, R. M. In Situ Exfoliated 2D Molybdenum Disulfide Analyzed by XPS. *Surf. Sci. Spectra* **2020**, *27*, No. 014019.
(43) Werfel, F.; Minni, E. Photoemission Study of the Electronic Structure of Mo and MO Oxides. *J. Phys. C: Solid State Phys.* **1983**, *16*, 6091−6100.
(44) Escalera-López, D.; Niu, Y.; Park, S. J.; Isaacs, M.; Wilson, K.; Palmer, R. E.; Rees, N. V. Hydrogen Evolution Enhancement of Ultra-Low Loading, Size-Selected Molybdenum Sulfide Nanoclusters by Sulfur Enrichment. *Appl. Catal., B* **2018**, *235*, 84−91.
(45) Benoist, L.; Gonbeau, D.; Pfister-Guillouzo, G.; Schmidt, E.; Meunier, G.; Levasseur, A. X-Ray Photoelectron Spectroscopy Characterization of Amorphous Molybdenum Oxysulfide Thin Films. *Thin Solid Films* **1995**, *258*, 110−114.
(46) Vrubel, H.; Hu, X. Growth and Activation of an Amorphous Molybdenum Sulfide Hydrogen Evolving Catalyst. *ACS Catal.* **2013**, *3*, 2002−2011.
(47) Sharma, J.; Iqbal, Z. X-Ray Photoelectron Spectroscopy of Brominated $(SN)_x$ and S_4N_4. *Chem. Phys. Lett.* **1978**, *56*, 373−376.
(48) Zhang, T.; Huang, J.; Xia, Y.; Zhao, R.; Sun, B.; Xiong, J.; Tao, B.; Wang, H.; Zhao, Y. A High-Efficiency Electrocatalyst for Hydrogen Evolution Based on Tree-Like Amorphous MoS_2 Nanostructures Prepared by Glancing Angle Deposition. *J. Solid State Chem.* **2020**, *286*, No. 121255.
(49) Banister, A. J.; Hauptman, Z. V.; Passmore, J.; Wong, C.-M.; White, P. S. Poly(Sulphur Nitride): An Assessment of the Synthesis from Trichlorocyclotri(Azathiene) and Trimethylsilyl Azide. *J. Chem. Soc., Dalton Trans.* **1986**, 2371−2379.
(50) Costa, M. B.; Medina, M.; Andrade, M. A. S., Jr.; Coelho, D.; Mascaro, L. H. Transition Metal Chalcogenides for Photoelectrochemical Water Splitting. *Photoelectrochemical Water Splitting*; Materials Research Foundations, 2020; Vol. *71*, pp 1−42.
(51) Kim, J. H.; Kim, H. E.; Kim, J. H.; Lee, J. S. Ferrites: Emerging Light Absorbers for Solar Water Splitting. *J. Mater. Chem. A* **2020**, *8*, 9447−9482.
(52) Morales-Guio, C. G.; Hu, X. Amorphous Molybdenum Sulfides as Hydrogen Evolution Catalysts. *Acc. Chem. Res.* **2014**, *47*, 2671−2681.
(53) Rohloff, M.; Cosgun, S.; Massué, C.; Lunkenbein, T.; Senyshyn, A.; Lerch, M.; Fischer, A.; Behrens, M. The Role of Synthesis Conditions for Structural Defects and Lattice Strain in β-TaON and Their Effect on Photo- and Photoelectrocatalysis. *Z. Naturforsch.* **2019**, *74*, 71−83.
(54) Le Formal, F. L.; Sivula, K.; Grätzel, M. The Transient Photocurrent and Photovoltage Behavior of a Hematite Photoanode under Working Conditions and the Influence of Surface Treatments. *J. Phys. Chem. C* **2012**, *116*, 26707−26720.
(55) Ma, Y.; Formal, F. L.; Kafizas, A.; Pendlebury, S. R.; Durrant, J. R. Efficient Suppression of Back Electron/Hole Recombination in Cobalt Phosphate Surface-Modified Undoped Bismuth Vanadate Photoanodes. *J. Mater. Chem. A* **2015**, *3*, 20649−20657.
(56) de Araújo, M. A.; Gromboni, M. F.; Marken, F.; Parker, S. C.; Peter, L. M.; Turner, J.; Aspinall, H. C.; Black, K.; Mascaro, L. H. Contrasting Transient Photocurrent Characteristics for Thin Films of Vacuum-Doped "Grey" TiO_2 and "Grey" Nb_2O_5. *Appl. Catal., B* **2018**, *237*, 339−352.
(57) Peter, L. M. Dynamic Aspects of Semiconductor Photoelectrochemistry. *Chem. Rev.* **1990**, *90*, 753−769.
(58) Zhao, J.; Cheng, Y.; Chen, Y.; Zhang, W.; Liu, E.; Fan, J.; Miao, H.; Hu, X. Defects Regulation of Sb_2S_3 by Construction of Sb_2S_3/In_2S_3 Direct Z-Scheme Heterojunction with Enhanced Photoelectrochemical Performance. *Appl. Surf. Sci.* **2021**, *568*, No. 150917.
(59) Chen, C.; Tang, J. Open-Circuit Voltage Loss of Antimony Chalcogenide Solar Cells: Status, Origin, and Possible Solutions. *ACS Energy Lett.* **2020**, *5*, 2294−2304.
(60) Choi, Y. C.; Lee, D. U.; Noh, J. H.; Kim, E. K.; Seok, I. S. Highly Improved Sb_2S_3 Sensitized-Inorganic−Organic Heterojunction Solar Cells and Quantifi Cation of Traps by Deep-Level Transient Spectroscopy. *Adv. Funct. Mater.* **2014**, *24*, 3587−3592.
(61) Bhushan, B. *Encyclopedia of Nanotechnology*; Springer, 2012.
(62) Nguyen, A. D.; Nguyen, T. K.; Le, C. T.; Kim, S.; Ullah, F.; Lee, Y.; Lee, S.; Kim, K.; Lee, D.; Park, S.; Bae, J.-S.; Jang, J. I.; Kim, Y. S. Nitrogen-Plasma-Treated Continuous Monolayer MoS_2 for Improving Hydrogen Evolution Reaction. *ACS Omega* **2019**, *4*, 21509−21515.
(63) Huang, P.-C.; Brahma, S.; Liu, P.-Y.; Huang, J.-L.; Wang, S.-C.; Weng, S.-C.; Shaikh, M. O. Atmospheric Air Plasma Treated SnS Films: An Efficient Electrocatalyst for HER. *Catalysts* **2018**, *8*, No. 462.
(64) Chen, Z.; Dinh, H. N.; Miller, E. *Photoelectrochemical Water Splitting Standards, Experimental Methods, and Protocols*; Springer, 2013.
(65) van de Krol, R.; Grätzel, M. *Photoelectrochemical Hydrogen Production*; Springer, 2012.
(66) Le Formal, F.; Tétreault, N.; Cornuz, M.; Moehl, T.; Grätzel, M.; Sivula, K. Passivating Surface States on Water Splitting Hematite Photoanodes with Alumina Overlayers. *Chem. Sci.* **2011**, *2*, 737−743.
(67) Yang, W.; Moehl, T.; Service, E.; Tilley, S. D. Operando Analysis of Semiconductor Junctions in Multi-Layered Photocathodes for Solar Water Splitting by Impedance Spectroscopy. *Adv. Energy Mater.* **2021**, *11*, No. 2003569.
(68) Li, Q.; Zheng, M.; Zhong, M.; Ma, L.; Wang, F.; Ma, L.; Shen, W. Engineering MoS_x/Ti/InP Hybrid Photocathode for Improved Solar Hydrogen Production. *Sci. Rep.* **2016**, *6*, No. 29738.
(69) Huang, Z.; Wang, C.; Pan, L.; Tian, F.; Zhang, X.; Zhang, C. Enhanced Photoelectrochemical Hydrogen Production Using Silicon Nanowires@MoS_3. *Nano Energy* **2013**, *2*, 1337−1346.
(70) Bard, A. J.; Memming, R.; Miller, B. Terminology in Semiconductor Electrochemistry and Photoelectrochemical Energy Conversion. *Pure Appl. Chem.* **1991**, *63*, 569−596.

https://doi.org/10.1021/acsaem.1c03374
ACS Appl. Energy Mater. 2022, 5, 1010−1022